OPEN ACCESS

University of BRISTOL

Publisher's PDF, also known as Version of record

License (if available):
Other

Link to published version (if available):
10.1029/2018GL081822

Link to publication record in Explore Bristol Research
PDF-document

University of Bristol - Explore Bristol Research
General rights

The Influence of Phenocrysts on Degassing in Crystal-Bearing Magmas With Rhyolitic Groundmass Melts

R. L. deGraffenried[1] , J. F. Larsen[2], N. A. Graham[2] , and K. V. Cashman[3]

[1]Department of Earth Sciences, School of Oceanography and Earth Science Technology, University of Hawai'i at Mānoa, Honolulu, HI, USA, [2]Department of Geosciences, College of Natural Science and Mathematics, University of Alaska Fairbanks, Fairbanks, AK, USA, [3]School of Earth Sciences, University of Bristol, Bristol, UK

Abstract The porosity at which a magma becomes permeable (i.e., the percolation threshold; ϕ_c) is important for magma degassing; it is also poorly constrained in crystal-bearing systems. To address this, we conduct high pressure-temperature decompression experiments on water-saturated rhyolitic melts with variable crystal contents. We find that crystal-bearing run products become permeable at ~55-vol.% vesicularity (crystal free), a value that is similar to that found in decompression-crystallization experiments using basaltic andesite compositions. Our results provide insight into controls on the eruption styles of hydrous, crystal-bearing magmas in general and controls on pulsatory Vulcanian behavior, in particular.

Plain Language Summary Rates of gas escape from an ascending magma control volcanic eruption style. Gas transport along permeable connected bubble pathways is an important step in the degassing process as it allows pressurized gases to escape. The bubble concentration at which permeability develops (the percolation threshold) is poorly characterized in magmas with moderate to high crystallinities. In this study, we use decompression experiments with controlled crystal contents to address this knowledge gap. Our results show that the presence of at least 20-vol.% crystals reduces the percolation threshold in crystal-bearing magmas compared to crystal-free magmas. This suggests that the presence of crystals will enhance gas escape during magma ascent and has implications for transitions between explosive and effusive eruption styles.

1. Introduction

The kinetics of gas escape from ascending magma has been extensively studied because magma degassing influences eruption style (e.g., Burgisser & Gardner, 2005; Eichelberger et al., 1986; Gonnermann & Manga, 2007; Klug & Cashman, 1996; Lindoo et al., 2016, 2017; Namiki & Manga, 2008; Rust & Cashman, 2011; Sparks, 2003). Eruptions of intermediate composition magma often cycle between lava dome extrusion, Vulcanian-style explosions and lava dome collapse (e.g., Coombs et al., 2010; Druitt et al., 2002; Kienle & Shaw, 1979; Power et al., 2006; Varley et al., 2010; Voight et al., 1999; Wright et al., 2012). Transitions in eruptive style are particularly challenging for hazard management and require improved understanding of how crystallization, volatile exsolution, degassing, and magma rise rates influence eruptive processes (Cashman & Sparks, 2013; Cassidy et al., 2018; Jaupart, 1998).

Vulcanian explosions are modulated by the formation and destruction of a dense, degassed magma plug within the conduit (Druitt et al., 2002). Plug failure initiates rapid, top-down evacuation of the conduit, generating an ash-rich eruption cloud that typically ascends to <10 km and is accompanied by pyroclastic density currents (Burgisser et al., 2010; Coombs et al., 2010; Giachetti et al., 2010; Isgett et al., 2017; Wright et al., 2007). Models of Vulcanian eruption cycles rely on accurate estimates of the conduit pressure and depth at which magma becomes permeable and degasses (Burgisser et al., 2010; Clarke et al., 2007; Diller et al., 2006; Isgett et al., 2017). Permeability initiates at a critical porosity (the percolation threshold; ϕ_c), when vesicle connectivity allows rapid gas loss from the magma. Estimates of ϕ_c range from 30 vol.% (Blower, 2001; Saar & Manga, 1999) to 80 vol.% (Lindoo et al., 2016; Takeuchi et al., 2008; Westrich & Eichelberger, 1994). In general, ϕ_c is high (~70 vol.%) for crystal-poor magmas experiencing rapid ascent and fragmentation and appears to be independent of melt viscosity (Lindoo et al., 2016; Rust & Cashman, 2011; Takeuchi et al., 2008). Studies focused on natural pyroclasts suggest that the presence of crystals can reduce ϕ_c (e.g., Wright et al., 2009), although experimental constraints on the permeability of crystal-bearing systems are limited (Lindoo et al., 2017; Martel & Iacono-Marziano, 2015; Okumura et al., 2012).

This study uses experiments to assess the influence of equant solid particles on ϕ_c in rhyolitic melts. Our results indicate that the addition of at least 20-vol.% particles decreases the critical porosity at which the system becomes permeable to gas from ~70 to ~55 vol.%. We then examine the role of decompression rate on permeability development and compare our experimental results to studies of well-observed Vulcanian eruptions. We show that the experimentally determined threshold agrees well with estimates of the vesicularity required to initiate Vulcanian-style explosions (Giachetti et al., 2010).

2. Methods

The experiments employed powdered rhyolite obsidian from Mono Craters, CA (76.3-wt.% SiO_2; Lindoo et al., 2016) seeded with equant corundum crystals (~355 μm; aspect ratio: 1.8 ± 0.6, $n = 64$, range: 1.1–3.5; after Okumura et al., 2012) to approximate a hydrous magma with rhyolite groundmass melt and phenocryst content similar to Augustine Volcano, USA, or Soufriere Hills Volcano, Montserrat (Larsen et al., 2010; Murphy et al., 1998). Seeding experiments with measured proportions of evenly distributed crystals required powdered starting glass. Three experimental series were conducted using 0-, 20-, and 40-vol.% corundum seed populations. The experiments were limited to a maximum of 40-vol.% seed crystals to maintain cohesion on quench. The starting materials and 5- to 7-wt.% deionized water were loaded into 5-mm-diameter silver (Ag) tubing with a separate 4-mm-diameter Ag inner capsule containing MgO powder as a sink to trap degassed vapor (after Burgisser & Gardner, 2005). The outer capsule was welded closed using a Puk 3 arc welder then checked by weighing after heating to 150 °C for at least 15 min.

The sealed capsules were loaded into TZM (Ti-Zr-Mo) or MHC (Mo-Hf-Carbide) pressure vessels fitted with water-cooled pressure seals. Methane gas was added to vessels to limit H diffusion through the capsule walls. Vessels were pressurized with Ar gas to 110 MPa, heated to 900 °C in a DelTech furnace, and held for 24 hr to saturate the starting materials in H_2O. Experiment MCO-NEQ-6 was not decompressed but was analyzed using Fourier transform infrared transmission spectroscopy to verify equilibrium saturation of the experiments, compared with a rhyolite solubility model (Moore et al., 1998).

Experimental pressure was monitored using a Heise gauge accurate to ±5 MPa. After holding for 24 hr, the experiments were decompressed isothermally and continuously at a rate of 0.25 ± 0.03 MPa/s to final pressures (P_f) between 90 and 15 MPa, equivalent to an ascent rate of ~9 m/s, assuming a lithostatic pressure gradient of 23 MPa/km. At each final pressure, the vessels were quenched within ~10 s of reaching P_f using the method of Sisson and Grove (1993).

Permeability measurements were conducted using a benchtop permeameter following Takeuchi et al. (2008) and Lindoo et al. (2016). Air flow rate was measured downstream using an Omega FMA-4000 digital mass flow meter, and the pressure drop across the sample was measured using a Testo 526 digital manometer. The Forchheimer equation (Rust & Cashman, 2004) allows Darcian (k_1) and intertial (k_2) permeabilities to be estimated as follows:

$$\frac{P_2^2 - P_1^2}{2P_0 L} = \frac{\mu}{k_1} v + \frac{\rho}{k_2} v^2, \tag{1}$$

where P_2 and P_1 are the pressures at the top and bottom of the sample and P_0 is the pressure at which air viscosity (μ) and velocity (v) are measured; typically $P_0 = P_1$. L is sample length, and ρ is fluid density.

Experimental porosities and bubble size distributions (BSDs) were measured using stereology (Russ, 1986) from reflected light or individual X-ray tomography images collected at the University of Texas High-Resolution X-Ray Computed Tomography Facility. Five to 10 images per sample at varying magnifications were analyzed using NIH ImageJ. The images were converted to binary, with crystal areas subtracted to determine melt-corrected porosities (e.g., Gurioli et al., 2005). Reflected light image montages were created with at least 40% image overlap, using Adobe Photoshop (e.g., Mongrain & Larsen, 2009). The resulting montage was analyzed three times, and the standard deviation between the measurements gives a typical measurement error of ±0.5-vol.% porosity.

A total of 66 to 1958 individual bubbles were measured from each image montage (Table 1) and converted to an equivalent radius, assuming spherical bubbles. Bubble number densities were calculated using stereological methods (Gardner et al., 1999; Mangan & Cashman, 1996).

3. Results

3.1. Bulk Properties: Crystal-Corrected Porosity and Bubble Number Density

As vesiculation progresses, the experimental porosities increase systematically with decreasing quench pressure (Table 1 and Figure 1a). The porosities are consistent with equilibrium porosities calculated for rhyolite melts at 900 °C (Gardner et al., 1999; Moore et al., 1998). At higher quench pressures, experimental porosities are systematically higher than the equilibrium curve by as much as 13 vol.% because of hydration bubbles inherited from the powdered material (e.g., Larsen & Gardner, 2000). At quench pressures below 50 MPa, the porosities agree well with the model, indicating H_2O exsolution at approximately equilibrium conditions.

Bubble number densities (N_V) in all three experimental series decrease with decreasing quench pressure, although data from seeded and unseeded experiments form two subparallel trends (Table 1 and Figure 1 b). The bubble populations coarsen at low pressures (75 to 20 MPa), as recorded by N_V decreases by ~1 order of magnitude. Unseeded and seeded experiments at 50 MPa have similar N_v within error (~17,000 to 20,000 bubbles per cubic centimeter); below 50 MPa, both 20- and 40-vol.% crystal-seeded experiments show N_v decreases by a factor of 2 (2,600–2,900 bubbles per cubic centimeter, seeded, compared with 6,400 bubbles per cubic centimeter, unseeded; Figure 1b). N_V converges toward a similar value (~2,200 bubbles per cubic centimeter) in each series as pressures approach 20 MPa.

3.2. BSDs

BSDs record the integrated effects of bubble nucleation, growth, and coalescence (Proussevitch et al., 2007). X-ray tomography images of experiments quenched at the lowest final pressures are shown in Figure 2a. The unseeded experiment (MCO-TNCM-7; P_f = 20 MPa; Figure 2a) has a relatively homogenous bubble population, whereas the 20- and 40-vol.% experiments (MCO-TCM-12 and MCO-TCM-4; P_f = 25 MPa; Figure 2a) show a subset of bubbles that are significantly larger and interspersed among seed crystals.

In all experimental series, most bubbles are small, with ~80% having radii ≤50 μm. At quench pressures between 75 and 30 MPa, the maximum bubble radii (R_{max}) are similar regardless of crystal content (Figure 2b). Below P_f = 30 MPa, R_{max} in the unseeded experiments increases to 508 μm between 25 and 20 MPa, whereas R_{max} in the seeded runs increases to 831 and 911 between 30 and 25 MPa. Thus, at low pressure, R_{max} is 1.6 to 1.8 times larger in seeded relative to unseeded experiments.

The experiments became permeable (k_1) at final pressures and porosities that correlate with the presence of crystals (Table 1 and Figure 3). The unseeded runs remained effectively impermeable ($k_1 < ~10^{-15}$ m^2; Lindoo et al., 2016) to 20 MPa, consistent with prior studies showing that crystal-free rhyolite experiments develop permeabilities at pressures of ~15 MPa and porosities of ~70 vol.% (Lindoo et al., 2016; Takeuchi et al., 2008). The crystal-seeded runs were effectively impermeable to P_f between 30 and 25 MPa. At 25 MPa, both crystal-bearing experimental series achieved measurable k_1 at ϕ_c ~ 55 to 56 vol.% (crystal corrected; Table 1 and Figure 3). Maximum measured permeabilities of log k_1 (m^2) = −12.81 ± 0.01 and log k_2 (m) = −9.72 ± 0.02 (MCO-TCM-26) were achieved at P_f = 15 MPa. Once ϕ_c was reached, experimental permeabilities increased with increasing vesicularity in both series to a maximum of 69 to 77 vol.% over the same pressure range (Figure 3).

4. Discussion

4.1. Permeability and Percolation Threshold

Experimental results suggest that magmas with rhyolitic groundmass melts and 20- to 40-vol.% phenocrysts will form an interconnected bubble network and become permeable at a ϕ_c ~ 55 vol.% (crystal corrected; bulk ϕ_c ~ 45 to 50 vol.%). When compared with similar experiments using basaltic andesite melts (Lindoo et al., 2017), our data suggest that the reduced ϕ_c applies regardless of crystal size, shape (aspect ratio ~2 to 8; this study; Lindoo et al., 2017), or melt composition (Lindoo et al., 2016). This result is surprising, because it suggests that ϕ_c reduction depends primarily on the presence of at least 20-vol.% crystals.

The University of Alaska Fairbanks (UAF) permeameter has a detection limit of ~10^{-15} m^2, as compared to 10^{-17} m^2 of Takeuchi et al. (2008), which means our estimated ϕ_c is a maximum. Significant magma

Table 1
Experimental Results

Sample	P_f (MPa)	ϕ (vol. %)[a]	log k_1 (m^2)[b,c]	log k_2 (m)	N_V (cm^{-3})[d]	n[e]	R_{max}[f] (μm)
0-vol.% crystals							
MCO-NEQ-6	110	13.9	B.D.L.	B.D.L.	11,867 (+/−427)	2,859	124
MCO-TNCM-13	75	21.1	B.D.L.	B.D.L.	29,062 (+3,007, −5,196)	1,958	90
MCO-TNCM-12	50	40.2	B.D.L.	B.D.L.	17,626 (+5,298, −3,483)	1,123	146
MCO-TNCM-4	25	62.9	B.D.L.	B.D.L.	6,393 (+1,778, −548)	309	334
MCO-TNCM-7	20	69.7	B.D.L.	B.D.L.	2,249 (+1,719, −1,008)	129	508
20-vol.% crystals							
MCO-TCM-37	90	9.1	B.D.L.	B.D.L.	n.d.[g]	n.d.	n.d.
MCO-TCM-5	75	30.1	B.D.L.	B.D.L.	12,110 (+1,658, −2,628)	370	127
MCO-TCM-36	65	34.7	B.D.L.	B.D.L.	n.d.	n.d.	n.d.
MCO-TCM-6	50	40.9	B.D.L.	B.D.L.	17,029 (+5,656, −8,032)	616	197
MCO-TCM-14	30	51.9	B.D.L.	B.D.L.	1,589 (+3,804, −761)	96	246
MCO-TCM-12	25	62.2	−13.48 (0.34)	−11.70 (0.05)	2,890 (+/−23)	1,123	911
MCO-TCM-20	25	54.9	B.D.L.	B.D.L.	n.d.	n.d.	n.d.
MCO-TCM-22	25	56.3	−13.52 (0.07)	−9.18 (0.25)	n.d.	n.d.	n.d.
MCO-TCM-33	20	77.4	−13.83 (0.12)	−10.23 (0.02)	n.d.	n.d.	n.d.
MCO-TCM-26	15	69.4	−12.82 (0.01)	−9.74 (0.02)	n.d.	n.d.	n.d.
40-vol.% crystals							
MCO-TCM-30	75	22.8	B.D.L.	B.D.L.	11,432 (+1,314, −1,973)	328	92
MCO-TCM-35	65	29.2	B.D.L.	B.D.L.	n.d.	n.d.	n.d.
MCO-TCM-2	50	41.2	B.D.L.	B.D.L.	19,870 (+951, −2,700)	228	161
MCO-TCM-13	30	51.9	B.D.L.	B.D.L.	3,292 (+1,464, −1,376)	66	270
MCO-TCM-4	25	57.1	−13.93 (0.06)	−11.13 (0.22)	2,602 (+100, −122)	343	831
MCO-TCM-27	25	60.5	−14.00 (0.03)	−11.48 (0.04)	n.d.	n.d.	n.d.
MCO-TCM-31	20	69.3	−14.18 (0.09)	−11.01 (0.03)	n.d.	n.d.	n.d.
MCO-TCM-17	15	69.3	−12.67 (0.10)	−10.48 (0.25)	n.d.	n.d.	n.d.

[a]Experimental porosities (ϕ) in volume % (vol. %). Errors on porosity are 0.5 vol.% determined as measurement error from stitched images after Mongrain and Larsen (2009).   [b]B.D.L means the measured permeability was below the detection limit of the laboratory permeameter.   [c]1σ standard deviation reported in parentheses.   [d]Bubble number density (N_V) in per cubic centimeter. Errors reported in parentheses.   [e]Total numbers of bubbles (n) measured in each sample.   [f]Largest bubble size (radius) in microns.   [g]n.d.—not determined for that sample.

degassing should occur when viscous (k_1) permeability reaches 10^{-15} m^2 (e.g., Clarke et al., 2007; Gonnermann et al., 2017; Takeuchi et al., 2005). We can approximate the relative effect of degassing at lower permeabilities using the characteristic timescale of permeable gas escape:
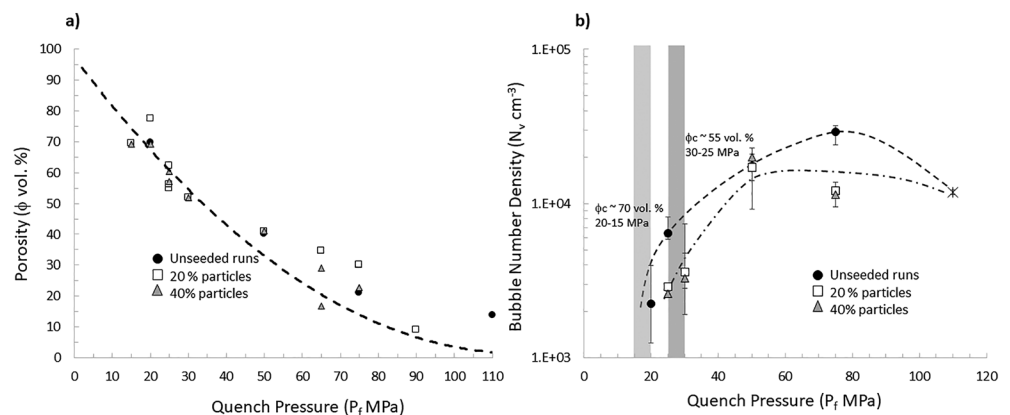

Figure 1. (a) Experimental porosities plotted as a function of quench pressure, in comparison with a modeled equilibrium porosity curve (dashed line: after Gardner et al., 1999; Moore et al., 1998). (b) Bubble number densities plotted as a function of quench pressure. The dashed lines are to guide the eye and are not quantitative models. The vertical shaded regions represent the pressure interval over which permeability developed in the unseeded, crystal-free experiments (light gray box; $\phi_c \sim$ 70-vol.% porosity; between 20 and 15 MPa; Lindoo et al., 2016) and in the 20- and 40-vol.% crystal-seeded experiments (dark gray shaded box; $\phi_c \sim$ 55-vol.% crystal-corrected porosity; between 30 and 25 MPa).
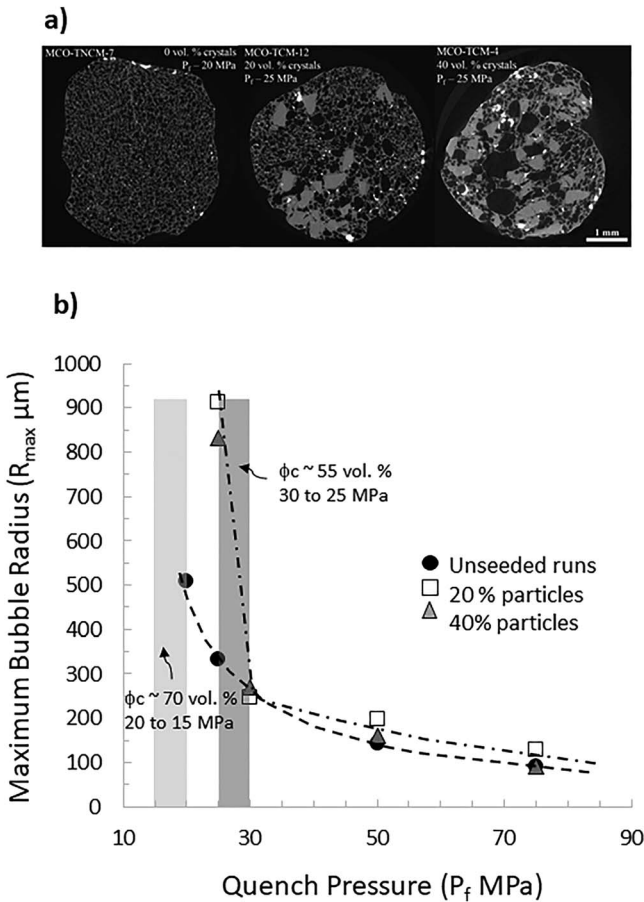
Figure 2. (a) Representative tomography images from each of the experiment series, from left to right: MCO-TNCM-7, 0-vol.% seed crystals, P_f = 20 MPa; MCO-TCM-12, 20-vol.% seed crystals, P_f = 25 MPa; MCO-TCM-4, 40-vol.% seed crystals, P_f = 25 MPa. In X-ray tomography, grayscale values represent relative phase density; black is void space, light gray are the corundum seed crystals, darker gray is glass, and the brightest phases are either Fe-Ti oxides (outside the bubbles) or vapor-condensed cristobalite (inside the bubbles; e.g., Horwell et al., 2013). The 1-mm scale bar is the same for all three images. Increasing coalescence as crystal content increases can be qualitatively observed in this sequence. (b) Largest bubble radii measured from the stitched reflected light image maps from experiments in each series. The vertical shaded boxes represent the pressure intervals over which permeability developed in each series: The light gray box represents ϕ_c ~ 70-vol.% porosity (between 20 and 15 MPa; Lindoo et al., 2016), and the dark gray box represents ϕ_c ~ 55-vol.% crystal-corrected porosity (between 30 and 25 MPa). The largest bubble radii in the 20- and 40-vol.% crystal-seeded experiments increase significantly in size relative to the unseeded experiments at a pressure of 30 MPa, by a factor of 1.6 to 1.8. The size increase correlates with the pressure interval over which those experiments become measurably permeable.

$$t = \frac{R^2 \mu_{gas}}{\Delta P k}, \qquad (2)$$

where t is time in seconds, R is the length scale over which gas escapes in meters, μ_{gas} is gas viscosity in pascal-seconds (10^{-5}; Rust & Cashman, 2011), ΔP is the pressure gradient driving gas escape in pascals, and k is the viscous permeability in square meters (Rust & Cashman, 2011). We consider effusive (0.2 m/s) and explosive (9 m/s) magma ascent rates, assume a length scale (conduit radius) of 10 m, and estimate ΔP as ~2.5×10^7 Pa, the pressure difference between 25 MPa (at which permeability develops) and 0.1 MPa (atmospheric pressure). If the conduit contains variably vesicular magma with a density of ~1,500 kg/m^3 (after Clarke et al., 2007), the rising magma should traverse the critical pressures in which permeability develops (30 to 25 MPa) in 10^3 and 10^1 s, respectively. Varying permeability only, the timescales of gas escape between the permeameter detection limits of 10^{-15} and 10^{-17} m^2 are 10^4 to 10^6 s, respectively. These timescales are minima because they assume the maximum pressure gradient; both are substantially longer, however, than the time required for a vesicular magma to cross the critical pressure threshold, so the difference in detection limit should not have an influence. Storage of permeable magma beneath a dense, impermeable plug would produce a smaller pressure gradient and increase the timescale of gas escape.

We extend this calculation to consider the timescale of gas escape relative to that of permeable magma ascent in the shallow conduit. Using the same magmastatic pressure gradient as above and rapid ascent (9 m/s), we estimate a timescale of ~10^2 s for a magma with permeability of k_1 ~ 10^{-13} m^2 (e.g., MCO-TCM-7) to ascend from the percolation threshold at 25 MPa to the fragmentation pressure at 10 MPa; the timescale for gas escape is also ~10^2 s, the same order of magnitude as the ascent timescale. However, for permeabilities <10^{-13} m^2, the gas escape timescale will be at least a factor of 10 longer than the ascent timescale. Thus, we conclude that high-permeability magmas and large conduit pressure gradients can generate gas escape rates equal to the ascent rate, relieving gas pressure. More commonly, though, vertical variations in permeability will decrease the driving pressure such that the gas loss timescale (>10^6 s) exceeds the timescale of magma ascent (e.g., Gonnermann & Manga, 2003).

4.2. The Influence of Crystals on Bubble Coalescence

The reduction in ϕ_c in crystal-bearing experiments is independent of melt viscosity, crystal size, and shape (Lindoo et al., 2016, 2017). Reduction in ϕ_c could reflect enhanced coalescence due to space limitations imposed by crystals. However, this implies that reductions in ϕ_c should scale with increasing crystal content, which we do not observe within the limits of our experimental method and permeameter detection limit. Alternatively, ϕ_c reduction could be tied to rheological behavior associated with increasing crystal content approaching random loose packing, which is ~20 vol.% for equant particles (Saar et al., 2001). Because our experiments did not exceed 40-vol.% seed crystals, we cannot explore how the approach to close packing (at ~60 vol.%; Saar et al., 2001) influences ϕ_c. Likely, if the particle shape is not equant (i.e., elongate or oblate), the necessary crystal content to induce a reduction in percolation threshold will change as these particle shapes have more pronounced rheological influences at more dilute concentrations (e.g., Lindoo et al., 2017; Mueller et al., 2009, 2011). Additionally, nonequant particle suspensions will be sensitive to pressure-
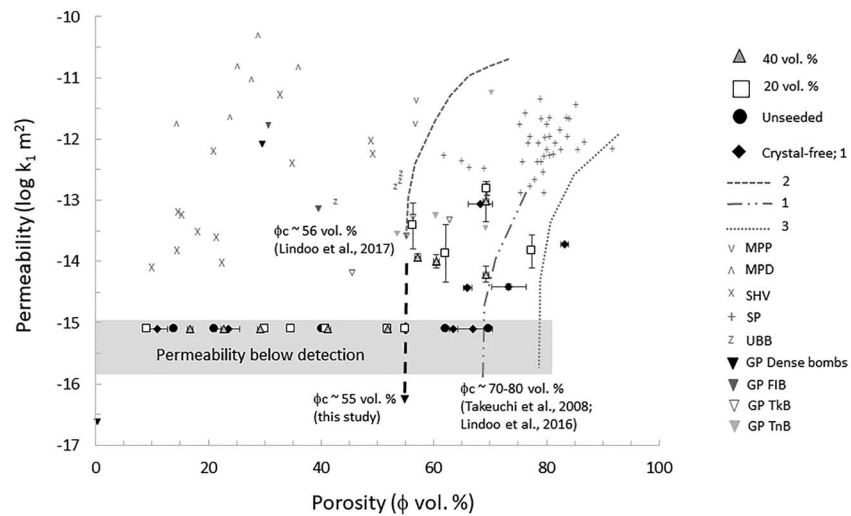
Figure 3. Porosity versus permeability (viscous, $\log k_1$, m^2) for the experiments from this study, in comparison with select experimental (line 3—Takeuchi et al., 2008; line 1—Lindoo et al., 2016; line 2—Lindoo et al., 2017) and natural samples. The shaded gray box represents the University of Alaska Fairbanks permeameter lower limit of detection, and samples within the field are effectively impermeable. The percolation threshold determined from this study (~55-vol.% crystal corrected) is denoted by the arrow. The experiments show the reduced percolation threshold constrained from experiments in comparison with crystal-rich natural samples from Soufriere Hills Volcano (SHV; gray xs; Melnik & Sparks, 2002), Mt. Pelee pumice and lava dome samples (MPP and MPD; gray v and upside down v symbols; Jouniaux et al., 2000), silicic Plinian pumice (SP; gray + symbol; Klug & Cashman, 1996), Unzen breadcrust bombs (UBB; gray z symbol; Mueller et al., 2005), and Guagua Pichincha breadcrust bombs and dense bombs (GP; upside down triangle symbols; Wright et al., 2007). The comparison samples were selected on the basis of eruption style (Vulcanian cycling and viscous, crystal-bearing lava dome samples) or as a crystal-free comparison (silicic pumice data).

volume changes during ascent as the deformation style of the system will vary depending on whether volume is adjusting to the pressure or the pressure is adjusting to the volume. Deformation influences the rheological contribution of nonequant particles as it controls the orientation of the particles; randomly oriented nonequant particles produce higher viscosity and higher yield strength suspensions than aligned nonequant particles (Cimarelli et al., 2011; Mueller et al., 2009). Our experiments represent the end member behavior of volume adjusting to a fixed pressure, which maximizes induced particle interactions.

Regardless of the precise mechanism of bubble-crystal interactions, numerical models (Degruyter et al., 2019; Parmigiani et al., 2016, 2017) demonstrate that rigid crystals confine bubbles during expansion, influencing bubble connectivity and reducing the percolation threshold. Confined bubble expansion, in turn, enhances bubble coalescence (Okumura et al., 2008). Bubbles are forced to expand toward each other in this case, which thins melt films between bubbles until the melt film reaches a critical thinness (<1 μm) and ruptures to form interconnected bubble pathways (Klug & Cashman, 1996; Mangan & Cashman, 1996; Klug et al., 2002). Experiments from Larsen et al. (2004) show that the timescale for this process is on the order of 10^1–10^2 s, as compared to 10^4–10^5 s for coalescence by drainage of melt from the films. In our experiments, the decreasing N_V with increasing porosity and decreasing quench pressure indicates coarsening bubble populations via coalescence, given the longer timescales needed for Ostwald ripening in viscous rhyolite melts (Castro et al., 2012; Larsen et al., 2004). Coalescence increases at $P_f \leq 30$ MPa, as illustrated by the significant increase in R_{max} (Figure 2b). Interestingly, this increase occurs at a pressure only ~5 MPa higher than the percolation threshold. Moreover, although there are only a few large bubbles in each experiment, they comprise >60% to 80% of the total gas volume and thus will significantly influence or even control degassing/outgassing processes.

One explanation for enhanced coalescence is porosity redistribution due to strain localization (Laumonier et al., 2011; Le Pennec et al., 2001). Deformation experiments conducted on experimentally created, crystal-bearing felsic magmas show concentration of pore spaces into shear bands when subjected to torsion (Laumonier et al., 2011). Gas focusing into pathways between rigid particle suspensions is also observed in analogue experiments (Oppenheimer et al., 2015). Although we cannot measure shear forces in our

experiments, it seems likely that modest shear forces caused by bubble expansion may force the gas + melt between seed crystals or capsule walls (e.g., Burgisser & Gardner, 2005; Lindoo et al., 2017) to form elongate bubbles (Figure 2a). We can, however, link a significant increase in maximum bubble size at P_f = 30 MPa to formation of a sample-spanning network of connected bubbles and permeability development by P_f = 25 MPa.

4.3. Application to Models of Vulcanian Eruptions

Key factors that modulate the effusive-explosive transition are the relative rates of magma ascent and outgassing; the latter is controlled by permeability threshold, permeability anisotropy, and the permeability of, and pressure at, the conduit walls (e.g., Diller et al., 2006; Jaupart, 1998; Schneider et al., 2012). Models of explosive Vulcanian eruptions typically describe a vertically stratified conduit capped by a dense and degassed, typically microcrystal-rich plug (~400 to 700 m deep; <7 to 13 MPa; Clarke et al., 2007; Diller et al., 2006). At constant magma ascent rates, plug thickness depends on the onset of outgassing, such that at lower ϕ_c, as observed in our crystal-bearing experiments, outgassing begins deeper in the conduit, which favors formation of a thicker plug (Diller et al., 2006). When magma ascent rates are variable, the plug thickness will be inversely proportional to the decompression rate (Diller et al., 2006). Eruptions will be explosive when gas pressure beneath the plug exceeds the plug strength (which we expect is proportional to its thickness) and effusive when the decompression rate is sufficiently slow that the plug strength is never exceeded.

Decompression rate is difficult to measure directly, but magma ascent rates have been estimated for explosive and effusive phases of several recent eruptions. For example, ascent rates during the Augustine 2006 eruption range from ~0.2 m/s during lava extrusion to ~2 to 5 m/s during explosions (Coombs et al., 2010); these rates equate to decompression rates of ~0.005 MPa/s and 0.046 to 0.115 MPa/s, respectively. The latter rates fall within the range of both our experiments (0.25 MPa/s) and those of Lindoo et al. (2017; 0.08 to 0.125 MPa/s), suggesting that experimental values of ϕ_c ~ 55 vol.% for crystal-bearing magmas can be applied to explosive phases of Vulcanian eruption cycles.

Recent work on bubble nucleation, growth, and coalescence in Soufriere Hills Volcano (SHV) samples from Vulcanian explosions in 1997 identified both preexplosion and synexplosion stages of vesiculation (Giachetti et al., 2010). SHV magmas are crystal-bearing andesites with 35- to 45-vol.% phenocrysts and rhyolitic matrix melts (Murphy et al., 1998) and are therefore similar to our experiments. The largest SHV bubble population, comprising 55-vol.% bulk porosity, is taken as the preexplosion gas content in the magma (Giachetti et al., 2010). This is in good agreement with the ϕ_c value determined in this study, although our value is based on crystal-subtracted porosity and the bulk porosities are ~5 to 10 vol.% lower (ϕ_c bulk ~45 to 50 vol.%). Similarly, our data correlate well with porosities and permeabilities measured from breadcrust bombs formed during Vulcanian eruptions of Guagua Pichincha volcano, Ecuador in 1999 (Wright et al., 2007), as well as breadcrust bombs from the 1991–1995 eruption of Unzen, Japan (Mueller et al., 2005; Figure 3); in both cases, $\log k_1 < -12.5 \, \text{m}^2$ and $\phi < 70$ vol.%. In contrast, $\phi_c \geq 70$ vol.% in crystal-poor experiments (this study; Lindoo et al., 2016), is similar to the high porosities and permeabilities measured from natural crystal-poor silicic pumice samples from Plinian eruptions (Klug & Cashman, 1996; Figure 3).

Our experimental results cannot be applied, however, to the porosity-permeability evolution of lavas produced by effusive dome-building eruptions or dense plugs, where samples have high permeabilities ($\log k_1 \leq -10.5 \, \text{m}^2$) at low porosities (<20 to 30 vol.%; Figure 3). These samples are often crystal rich (>50 vol.%), and electrical conductivity measurements show that pore microstructures are dominated by crack-like features (Le Pennec et al., 2001; Wright et al., 2009; Larsen, unpub. data). We thus conclude that our experiments are representative of conditions in the conduit prior to brittle deformation that causes microfracturing in natural magmas. Additionally, we can conclude that it is unlikely our experiments were thermally fractured during quench, as measured permeability-porosity relationships are consistent with gas flow along connected bubble pathways, not cracks.

More generally, the growing body of experimental results suggests that crystals exert a strong influence on magma degassing, consistent with sample-based interpretations of degassing processes operating in crystal-bearing and crystal-poor magmas (Figure 3). Crystal-enhanced degassing is particularly important for determining the timing of Vulcanian eruption cycles, which is modulated by the relative rates of magma ascent and degassing, which in turn control the rate of shallow plug formation and failure. Importantly,

crystallization of hydrous intermediate composition magmas is controlled by the efficacy of volatile exsolution from the melt and the kinetics of crystal formation in response to degassing (e.g., Hammer & Rutherford, 2002). Thus, the explosive-effusive transition of intermediate volcanoes is determined by numerous feedbacks involving pressure-driven variations in the bubble and crystal populations (e.g., Cassidy et al., 2018).

5. Conclusions

This study examines the critical porosity at which permeability develops in phenocryst-bearing magmas (20 to 40 vol.%) with rhyolite groundmass melts through three decompression experimental series. The ϕ_c estimated from crystal-seeded experiments is ~55 vol.% (crystal corrected; $P_f \leq 25$ MPa) and is independent of crystal content for the studied range, which is consistent with prior experimental results (Lindoo et al., 2017).

Our results can be applied to Vulcanian eruption models and sample-based interpretations of conduit stratigraphy. Preexplosion magma vesicularities of ~55 vol.% (bulk) estimated for the conduit transition region beneath a dense, variably degassed plug (Giachetti et al., 2010) agree well with our experimentally determined ϕ_c (55-vol.% crystal-corrected or 45- to 50-vol.% bulk porosity). The crystal-seeded experiments developed permeability at pressures between 30 and 25 MPa, corresponding to a conduit depth of 1.7 km, assuming a variably vesicular magma overburden (~1,500-kg/m^3 bulk density, after Clarke et al., 2007). This value is similar to the evacuation depth estimated for Vulcanian explosions at Guagua Pichincha (1.5 km; Wright et al., 2007). Finally, although magma ascent/decompression rate is likely the dominant control on Vulcanian explosion cycles, our experiments suggest that a decrease in ϕ_c caused by moderate crystallinity may create a thicker plug (Diller et al., 2006), which could help modulate both repose time between explosions and the strength of the explosion itself.

References

Blower, J. (2001). Factors controlling permeability–porosity relationships in magma. *Bulletin of Volcanology*, *63*(7), 497–504.

Burgisser, A., & Gardner, J. E. (2005). Experimental constraints on degassing and permeability in volcanic conduit flow. *Bulletin of Volcanology*, *67*(1), 42–56.

Burgisser, A., Poussineau, S., Arbaret, L., Druitt, T. H., Giachetti, T., & Bourdier, J. L. (2010). Pre-explosive conduit conditions of the 1997 Vulcanian explosions at Soufrière Hills Volcano, Montserrat: I. Pressure and vesicularity distributions. *Journal of Volcanology and Geothermal Research*, *194*(1), 27–41.

Cashman, K. V., & Sparks, R. S. J. (2013). How volcanoes work: A 25 year perspective. *Geological Society of America Bulletin*, *125*(5-6), 664–690.

Cassidy, M., Manga, M., Cashman, K., & Bachmann, O. (2018). Controls on explosive-effusive volcanic eruption styles. *Nature Communications*, *9*(1), 2839.

Castro, J. M., Burgisser, A., Schipper, C. I., & Mancini, S. (2012). Mechanisms of bubble coalescence in silicic magmas. *Bulletin of Volcanology*, *74*(10), 2339–2352.

Cimarelli, C., Costa, A., Mueller, S., & Mader, H. M. (2011). Rheology of magmas with bimodal crystal size and shape distributions: Insights from analog experiments. *Geochemistry, Geophysics, Geosystems*, *12*, Q07024. https://doi.org/10.1029/2011GC003606

Clarke, A. B., Stephens, S., Teasdale, R., Sparks, R. S. J., & Diller, K. (2007). Petrologic constraints on the decompression history of magma prior to Vulcanian explosions at the Soufrière Hills volcano, Montserrat. *Journal of Volcanology and Geothermal Research*, *161*(4), 261–274.

Coombs, M. L., Bull, K. F., Vallance, J. W., Schneider, D. J., Rhoms, E. E., Wessels, R. L., & McGimsey, R. G. (2010). Timing, distribution, and volume of proximal products of the 2006 eruption of Augustine Volcano. In J. A. Power, M. L. Coombs, & J. T. Freymueller (Eds.), *The 2006 eruption of Augustine Volcano, Alaska*, *USGS Prof. Paper*, (Vol. 1769, pp. 145–186).

Degruyter, W., Parmigiani, A., Huber, C., & Bachmann, O. (2019). How do volatiles escape their shallow magmatic hearth? *Philosophical Transactions of the Royal Society A*, *377*.

Diller, K., Clarke, A. B., Voight, B., & Neri, A. (2006). Mechanisms of conduit plug formation: Implications for vulcanian explosions. *Geophysical Research Letters*, *33*, L20302. https://doi.org/10.1029/2006GL027391

Druitt, T. H., Young, S. R., Baptie, B., Bonadonna, C., Calder, E. S., Clarke, A. B., et al. (2002). Episodes of cyclic Vulcanian explosive activity with fountain collapse at Soufrière Hills Volcano, Montserrat. *Memoirs. Geological Society of London*, *21*, 281–306.

Eichelberger, J. C., Carrigan, C. R., Westrich, H. R., & Price, R. H. (1986). Non-explosive silicic volcanism. *Nature*, *323*(6089), 598–602.

Gardner, J. E., Hilton, M., & Carroll, M. R. (1999). Experimental constraints on degassing of magma: Isothermal bubble growth during continuous decompression from high pressure. *Earth and Planetary Science Letters*, *168*(1), 201–218.

Giachetti, T., Druitt, T. H., Burgisser, A., Arbaret, L., & Galven, C. (2010). Bubble nucleation, growth and coalescence during the 1997 Vulcanian explosions of Soufrière Hills Volcano, Montserrat. *Journal of Volcanology and Geothermal Research*, *193*(3-4), 215–231.

Gonnermann, H., Giachetti, T., Fliedner, C., Nguyen, C. T., Houghton, B. F., Crozier, J. A., & Carey, R. J. (2017). Permeability during magma expansion and compaction. *Journal of Geophysical Research: Solid Earth*, *122*, 9825–9848. https://doi.org/10.1002/2017JB014783

Gonnermann, H. M., & Manga, M. (2007). The fluid mechanics inside a volcano. *Annual Review of Fluid Mechanics*, *39*, 321–356.

Gonnermann, H. M., & Manga, M. (2003). Explosive volcanism may not be an inevitable consequence of magma fragmentation. *Nature*, *426*(6965), 432.

Gurioli, L., Houghton, B. F., Cashman, K. V., & Cioni, R. (2005). Complex changes in eruption dynamics during the 79 AD eruption of Vesuvius. *Bulletin of Volcanology*, *67*(2), 144–159.

Hammer, J. E., & Rutherford, M. J. (2002). An experimental study of the kinetics of decompression-induced crystallization in silicic melt. *Journal of Geophysical Research*, *107*(B1), 2021. https://doi.org/10.1029/2001JB000281

Horwell, C. J., Williamson, B. J., Llewellin, E. W., Damby, D. E., & Le Blond, J. S. (2013). The nature and formation of cristobalite at the Soufrière Hills volcano, Montserrat: Implications for the petrology and stability of silicic lava domes. *Bulletin of Volcanology*, *75*(3), 696.

Isgett, S. J., Houghton, B. F., Fagents, S. A., Biass, S., Burgisser, A., & Arbaret, L. (2017). Eruptive and shallow conduit dynamics during Vulcanian explosions: Insights from the Episode IV block field of the 1912 eruption of Novarupta, Alaska. *Bulletin of Volcanology*, *79*(8), 58.

Jaupart, C. (1998). Gas loss from magmas through conduit walls during eruption. *Geological Society, London, Special Publications*, *145*(1), 73–90.

Jouniaux, L., Bernard, M. L., Zamora, M., & Pozzi, J. P. (2000). Streaming potential in volcanic rocks from Mount Pelée. *Journal of Geophysical Research*, *105*(B4), 8391–8401.

Kienle, J., & Shaw, G. E. (1979). Plume dynamics, thermal energy and long-distance transport of vulcanian eruption clouds from Augustine volcano, Alaska. *Journal of Volcanology and Geothermal Research*, *6*(1-2), 139–164.

Klug, C., Cashman, K., & Bacon, C. (2002). Structure and physical characteristics of pumice from the climactic eruption of Mount Mazama (Crater Lake), Oregon. *Bulletin of Volcanology*, *64*(7), 486–501.

Klug, C., & Cashman, K. V. (1996). Permeability development in vesiculating magmas: Implications for fragmentation. *Bulletin of Volcanology*, *58*(2), 87–100.

Larsen, J. F., Denis, M. H., & Gardner, J. E. (2004). Experimental study of bubble coalescence in rhyolitic and phonolitic melts. *Geochimica et Cosmochimica Acta*, *68*(2), 333–344.

Larsen, J. F., & Gardner, J. E. (2000). Experimental constraints on bubble interactions in rhyolite melts: Implications for vesicle size distributions. *Earth and Planetary Science Letters*, *180*(1), 201–214.

Larsen, J. F., Nye, C. J., Coombs, M. L., Tilman, M., Izbekov, P., & Cameron, C. (2010). Petrology and geochemistry of the 2006 eruption of Augustine Volcano. In J. A. Power, M. L. Coombs, & J. T. Freymueller (Eds.), *The 2006 eruption of Augustine Volcano, Alaska*, *USGS Prof. Paper*, (Vol. 1769, pp. 335–382).

Laumonier, M., Arbaret, L., Burgisser, A., & Champallier, R. (2011). Porosity redistribution enhanced by strain localization in crystal-rich magmas. *Geology*, *39*(8), 715–718.

Le Pennec, J. L., Hermitte, D., Dana, I., Pezard, P., Coulon, C., Cochemé, J. J., et al. (2001). Electrical conductivity and pore-space topology of Merapi Lavas: Implications for the degassing of porphyritic andesite magmas. *Geophysical Research Letters*, *28*(22), 4283–4286. https://doi.org/10.1029/2001GL013401

Lindoo, A., Larsen, J. F., Cashman, K. V., & Oppenheimer, J. (2017). Crystal controls on permeability development and degassing in basaltic andesite magma. *Geology*, *45*(9), 831–834.

Lindoo, A. N., Larsen, J. F., Cashman, K. V., Dunn, A. L., & Neill, O. K. (2016). An experimental study of permeability development as a function of crystal-free melt viscosity. *Earth and Planetary Science Letters*, *435*, 45–54.

Mangan, M. T., & Cashman, K. V. (1996). The structure of basaltic scoria and reticulite and inferences for vesiculation, foam formation, and fragmentation in lava fountains. *Journal of Volcanology and Geothermal Research*, *73*(1-2), 1–18.

Martel, C., & Iacono-Marziano, G. (2015). Timescales of bubble coalescence, outgassing, and foam collapse in decompressed rhyolitic melts. *Earth and Planetary Science Letters*, *412*, 173–185.

Melnik, O., & Sparks, R. S. J. (2002). Dynamics of magma ascent and lava extrusion at Soufrière Hills Volcano, Montserrat. *Geological Society, London, Memoirs*, *21*(1), 153–171.

Mongrain, J., & Larsen, J. F. (2009). Spatial point pattern analysis applied to bubble nucleation in silicate melts. *Computers & Geosciences*, *35*(9), 1917–1924.

Moore, G., Vennemann, T., & Carmichael, I. S. E. (1998). An empirical model for the solubility of H_2O in magmas to 3 kilobars. *American Mineralogist*, *83*(1), 36–42.

Mueller, S., Llewellin, E. W., & Mader, H. M. (2009). The rheology of suspensions of solid particles. *Proceedings of the Royal Society A: Mathematical, Physical and Engineering Sciences*, *466*(2116), 1201–1228.

Mueller, S., Llewellin, E. W., & Mader, H. M. (2011). The effect of particle shape on suspension viscosity and implications for magmatic flows. *Geophysical Research Letters*, *38*, L13316. https://doi.org/10.1029/2011GL047167

Mueller, S., Melnik, O., Spieler, O., Scheu, B., & Dingwell, D. B. (2005). Permeability and degassing of dome lavas undergoing rapid decompression: An experimental determination. *Bulletin of Volcanology*, *67*(6), 526–538.

Murphy, M. D., Sparks, R. S. J., Barclay, J., Carroll, M. R., Lejeune, A. M., Brewer, T. S., et al. (1998). The role of magma mixing in triggering the current eruption at the Soufriere Hills volcano, Montserrat, West Indies. *Geophysical Research Letters*, *25*(18), 3433–3436. https://doi.org/10.1029/98GL00713

Namiki, A., & Manga, M. (2008). Transition between fragmentation and permeable outgassing of low viscosity magmas. *Journal of Volcanology and Geothermal Research*, *169*(1-2), 48–60.

Okumura, S., Nakamura, M., Nakano, T., Uesugi, K., & Tsuchiyama, A. (2012). Experimental constraints on permeable gas transport in crystalline silicic magmas. *Contributions to Mineralogy and Petrology*, *164*(3), 493–504.

Okumura, S., Nakamura, M., Tsuchiyama, A., Nakano, T., & Uesugi, K. (2008). Evolution of bubble microstructure in sheared rhyolite: Formation of a channel-like bubble network. *Journal of Geophysical Research*, *113*, B07208. https://doi.org/10.1029/2007JB005362

Oppenheimer, J., Rust, A. C., Cashman, K. V., & Sandnes, B. (2015). Gas migration regimes and outgassing in particle-rich suspensions. *Frontiers in Physics*, *3*, 60.

Parmigiani, A., Degruyter, W., Leclaire, S., Huber, C., & Bachmann, O. (2017). The mechanics of shallow magma reservoir outgassing. *Geochemistry, Geophysics, Geosystems*, *18*, 2887–2905. https://doi.org/10.1002/2017GC006912

Parmigiani, A., Faroughi, S., Huber, C., Bachmann, O., & Su, Y. (2016). Bubble accumulation and its role in the evolution of magma reservoirs in the upper crust. *Nature*, *532*, 492–495.

Power, J. A., Nye, C. J., Coombs, M. L., Wessels, R. L., Cervelli, P. F., Dehn, J., et al. (2006). The reawakening of Alaska's Augustine volcano. *Eos, Transactions American Geophysical Union*, *87*(37), 373–377.

Proussevitch, A. A., Sahagian, D. L., & Tsentalovich, E. P. (2007). Statistical analysis of bubble and crystal size distributions: Formulations and procedures. *Journal of Volcanology and Geothermal Research*, *164*(3), 95–111.

Russ, J. C. (1986). *Practical stereology*. New York City: Springer Science & Business Media.

Rust, A. C., & Cashman, K. V. (2004). Permeability of vesicular silicic magma: Inertial and hysteresis effects. *Earth and Planetary Science Letters*, *228*(1), 93–107.

Rust, A. C., & Cashman, K. V. (2011). Permeability controls on expansion and size distributions of pyroclasts. *Journal of Geophysical Research*, *116*, B11202. https://doi.org/10.1029/2011JB008494

Saar, M. O., & Manga, M. (1999). Permeability-porosity relationship in vesicular basalts. *Geophysical Research Letters*, *26*(1), 111–114.

Saar, M. O., Manga, M., Cashman, K. V., & Fremouw, S. (2001). Numerical models of the onset of yield strength in crystal–melt suspensions. *Earth and Planetary Science Letters*, *187*(3-4), 367–379.

Schneider, A., Rempel, A. W., & Cashman, K. V. (2012). Conduit degassing and thermal controls on eruption styles at Mount St. Helens. *Earth and Planetary Science Letters*, *357*, 347–354.

Sisson, T. W., & Grove, T. L. (1993). Experimental investigations of the role of H_2O in calc-alkaline differentiation and subduction zone magmatism. *Contributions to Mineralogy and Petrology*, *113*(2), 143–166.

Sparks, R. S. J. (2003). Dynamics of magma degassing. *Geological Society, London, Special Publications*, *213*(1), 5–22.

Takeuchi, S., Nakashima, S., & Tomiya, A. (2008). Permeability measurements of natural and experimental volcanic materials with a simple permeameter: toward an understanding of magmatic degassing processes. *Journal of Volcanology and Geothermal Research*, *177*(2), 329–339.

Takeuchi, S., Nakashima, S., Tomiya, A., & Shinohara, H. (2005). Experimental constraints on the low gas permeability of vesicular magma during decompression. *Geophysical Research Letters*, *32*, L10312. https://doi.org/10.1029/2005GL022491

Varley, N., Arámbula-Mendoza, R., Reyes-Dávila, G., Sanderson, R., & Stevenson, J. (2010). Generation of Vulcanian activity and long-period seismicity at Volcán de Colima, Mexico. *Journal of Volcanology and Geothermal Research*, *198*(1-2), 45–56.

Voight, B., Sparks, R. S. J., Miller, A. D., Stewart, R. C., Hoblitt, R. P., Clarke, A., et al. (1999). Magma flow instability and cyclic activity at Soufriere Hills volcano, Montserrat, British West Indies. *Science*, *283*(5405), 1138–1142.

Westrich, H. R., & Eichelberger, J. C. (1994). Gas transport and bubble collapse in rhyolitic magma: an experimental approach. *Bulletin of Volcanology*, *56*(6-7), 447–458.

Wright, H. M., Cashman, K. V., Gottesfeld, E. H., & Roberts, J. J. (2009). Pore structure of volcanic clasts: Measurements of permeability and electrical conductivity. *Earth and Planetary Science Letters*, *280*(1), 93–104.

Wright, H. M., Cashman, K. V., Mothes, P. A., Hall, M. L., Ruiz, A. G., & Le Pennec, J. L. (2012). Estimating rates of decompression from textures of erupted ash particles produced by 1999–2006 eruptions of Tungurahua volcano, Ecuador. *Geology*, *40*(7), 619–622.

Wright, H. M., Cashman, K. V., Rosi, M., & Cioni, R. (2007). Breadcrust bombs as indicators of Vulcanian eruption dynamics at Guagua Pichincha volcano, Ecuador. *Bulletin of Volcanology*, *69*(3), 281–300.